Geotech Geol Eng (2020) 38:2427–2445
https://doi.org/10.1007/s10706-019-01160-0

ORIGINAL PAPER

Numerical Study on the Interaction Between Debris Flow Slurry and Check Dams Based on Fluid–Solid Coupling Theory

Xianbin Yu · Xiaoqing Chen · Honglong Wang · Chuanyang Jia

Received: 23 October 2019 / Accepted: 16 December 2019 / Published online: 23 December 2019

Abstract In order to effectively prevent and control debris flow disasters, it is one of the most effective engineering measures to construct a blocking project in the valley section of the circulation section to actively reduce the flow and velocity of debris flow. The check dams is taken as a control structure to intercept the solid materials of flush flood and debris flow in the channel, which play an important role in debris flow prevention and control project. However, the huge impact force of debris flow often causes the check dam to be destroyed. Based on the theory of fluid–solid coupling, by means of structural dynamics simulation software, fluid dynamics simulation software and coupling plane data transfer software, numerical simulation of the interaction between debris flow and the check dam has been carried out. Research results indicate that (1) the overflow section is subjected to the impact of the debris flow greater than the abutment; (2) debris flow impact only has a greater impact on a certain depth of the check dam, and the impact beyond this range is less. The numerical simulation results can provide data support for the design and optimization of the check dam.

Keywords Fluid–solid coupling · Bingham model · Debris flow impact force · Dynamic response

X. Yu (✉) · H. Wang · C. Jia
School of Civil Engineering and Architecture, Linyi University, Linyi 276000, China
e-mail: yuxianbin2006@126.com

X. Yu · X. Chen
Key Laboratory of Mountain Hazards and Surface Processes, Institute of Mountain Hazards and Environment, Chinese Academy of Sciences, Chengdu 610041, China

X. Yu
Linyi City Key Lab of Appraisement and Strengthening in Building Structures, Linyi 276000, China

X. Yu
Linyi City Engineering Technology Research Center of the Sponge City, Linyi 276000, China

1 Introduction

Debris flow disaster is huge, threatening the lives and property living in mountainous areas around the world (Hübl et al. 2009). The upstream debris flow prevention and control project can effectively reduce the damage of debris flow to downstream life and buildings. Debris flow mainly causes damage through three methods: erosion, siltation and direct impact. What is more, the impact force of debris flow is the main way to cause damage to buildings (structures) in the area affected by debris flow (Moriguchi et al. 2009). The impact force of debris flows refers to a dynamic load produced by a moving debris flow process that contacts other objects; this major external force causes engineering damage to the debris flow areas of roads, bridges, and housing projects (Chen

et al. 2007; Liu and Wei 1997). A debris flow is a typical solid–liquid two-phase flow. In the process of debris flow movement, the flow carries a wide particle size distribution of solid particles ranging from a few millimeters to tens of dollars. For this reason, it is difficult to use density, velocity, or deep mud to explain the differences in conditions of debris flow impacts (Hu et al. 2011). Moreover, because of the randomness of the impacting solid particles, the impact force of the debris flow is not the same under the same conditions at different locations (Iverson et al. 2010), further increasing the difficulty of studying the debris flow impact force. Over the years, determining the debris flow characteristics and impact load has been scientifically difficult, and this is still the weakness of debris flow dynamics (Chen et al. 2008; Cui 2009). The main methods of obtaining debris flow impact force data include field measurements, model tests and numerical simulation. Both domestic and overseas scholars have used field in situ experiments and indoor model experiments to study the impact force of debris flow (Okuda and Okunishi 1980; Zhang and Yuan 1985; Wu et al. 1990; König 2006; Wendeler et al. 2007; DeNatale et al. 1999; Bugnion et al. 2012a, b; Scheidl et al. 2013; Wei 1996; Armanini and Scotton 1993; He et al. 2013; He et al. 2014a; b; Yang et al. 2011; Tang et al. 2013; Cui et al. 2015; Zeng 2014; Zeng et al. 2015; Lei et al. 2018; Valentino et al. 2008). However, most of the experiments can only study the characteristics of the impact force of the debris flow, and it is rare to analyze the force of the blocking structure. Based on the fluid–solid coupling theory, numerical simulation is a good way to study the interaction between debris flow and retaining structure. Hillslope debris flow and channelized debris flow was firstly carried by experiments, and then defining the debris flow as a single-phase uniform flow, the coupling between debris flow and bank slope was studied by the commercial finite element calculation software (Chen et al. 2007). Based on the three-dimensional finite element nonlinear fluid–solid coupling analysis, the numerical simulation method is used to study the motion state of open channel fluids (Liu and Shu 2003). A more comprehensive fluid–solid coupling model was proposed (Bathe 2003). A hybrid computational framework was presented, using a total Lagrangian formulation of the Finite Element Method (FEM) to represent a flexible barrier. The actions exerted on the structure by a debris flow were obtained from simultaneous simulations of the flow of a fluid–grain mixture, using two conveniently coupled solvers: the discrete element method (DEM) governed the motion of the grains, while the free-surface non-Newtonian fluid phase was solved using the Lattice–Boltzmann method (LBM) (Leonardi et al. 2015; Leonardi 2015). Based on the basic theory of fluid–solid coupling, coupling analysis of debris flow and channel was carried out by commercial software (Li et al. 2008). Based on the theory of fluid–solid coupling, the debris flow is treated as a single-phase uniform flow, and the dynamic response of the masonry structure under the impact of debris flow under different working conditions was numerically simulated (Chen et al. 2013). However, most of the above studies do not consider the two-way coupling of debris flow and structure.

The problem of coupling between debris flow and sand dam is a problem of interaction between fluid and structural plane. However, due to the inclusion of more solid particles in the debris flow and the wide distribution of the particles, it is difficult to establish the real coupling between the debris flow and the check dam. In this work, the debris fluid is treated as a single-phase homogeneous fluid. The fluid dynamics calculation software and the structural dynamics calculation software are used to calculate the fluid and solid domains respectively. The debris flow is realized by calling the multi-physical coupling tool. The real-time exchange of each analysis step of the pressure of the fluid domain node and the displacement of the stress field of the check dam realizes the true bidirectional flow-solid coupling of the debris fluid and the check dam.

2 Mathematical Mechanics Model of Fluid–Solid Coupling

2.1 Governing Equations of Debris Flow

This study concerns incompressible fluids which are governed by the continuity equation

$$\nabla \cdot \mathbf{u} = 0 \tag{1}$$

and the momentum equation

$$\frac{\partial(\rho \mathbf{u})}{\partial t} + \rho \nabla \cdot \mathbf{u}\mathbf{u} = -\nabla p + \nabla \boldsymbol{\tau} \tag{2}$$

where **u** is the velocity, p is the pressure is the deviatoric stress tensor and the gravity contribution is incorporated in the pressure. All equations are written in a coordinate free form.

The stress tensor obeys the following law for Bingham fluids model.

$$\begin{cases} \tau = 2\left(\mu|\dot{\gamma}| + \dfrac{\tau}{|\dot{\gamma}|}\right)\mathbf{D}, & |\tau| > \tau_0 \\ \mathbf{D} = 0, & |\tau| \le \tau_0 \end{cases} \tag{3}$$

where τ is the yield stress and $\mu \ge 0$. For the yield stress models $|\tau|$ is the second invariant of the deviatoric stress tensor

$$|\tau| = \left(\tau_{ij}\tau_{ij}/2\right)^{0.5} \tag{4}$$

$\dot{\gamma}$ is the shear rate obtained from the following definition involving the second invariant of the rate of deformation tensor

$$\dot{\gamma} = \left(\mathbf{D}_{ij}\mathbf{D}_{ij}/_2\right)^{0.5} \tag{5}$$

with the rate of strain tensor D given by

$$\mathbf{D} = \frac{1}{2}\left([\nabla \mathbf{u}] + [\nabla \mathbf{u}]^{\mathrm{T}}\right) \tag{6}$$

2.2 Mathematical Mechanics Model of the Check dam

Mathematical mechanics model of the check dam has the following three group equations.

2.2.1 Equilibrium Differential Equations

$$\sigma_{ij,i} + f_j = \rho \frac{\partial^2 v_j}{\partial t^2} \tag{7}$$

where σ_{ij} is the normal or shear stress, t is the time, f_i is volume force and v_j is the velocity of the solid domain. If the solid domain remains immobile, v_j is equal to zero. The equilibrium differential equation can be expressed as follows:

$$\sigma_{ij,i} + f_j = 0 \tag{8}$$

2.2.2 Geometric Equations

$$\varepsilon_{ij} = \frac{1}{2}\left(w_{i,j} + w_{j,i}\right) \tag{9}$$

where $\tau\tau_{\tau\tau\tau\tau}$ is the normal or shear strain and w is the displacement.

2.2.3 Physical Equations

Incremental form of constitutive equations of deformation field of the check dam can be expressed as follow:

$$\left\{d\sigma_{ij}^{'}\right\} = \left[D_{\mathrm{eq}}\right]\left\{d\varepsilon_{ij}\right\} \tag{10}$$

where $d\sigma_{ij}^{'}$ the effective stress increment and $\left[D_{\mathrm{eq}}\right]$ is the elastic–plastic matrix.

2.3 Satisfying Relation of the Coupling Interface Between the Flow Field and the Stress Field

Based on the results of previous studies, it is known that fluid–solid coupling problems can be divided into the following two types according to their coupling positions. The one problem is the coupling action occurs only at the two intersection interface, and the other is the fluid and solid domains partially or completely overlap, which is hard to be clearly separated. Whether it is the first kind of problem or the second, the following two conditions should be satisfied on the fluid–solid coupling interface.

Displacement consistency:

$$d_f = d_s \tag{11}$$

Traction balance:

$$f_f = f_s \tag{12}$$

where d_s is displacement of solid domain, d_f is displacement of fluid domain, f_s is traction force of solid domain and f_f is traction force of fluid domain.

The above equations constitute a mathematical model of fluid–structure interaction, and solving for a particular problem must also include fluid boundary and check dams stress field boundary.

2.4 Boundary Conditions

2.4.1 Boundary Conditions of Fluid Field

Firstly, inlet boundary condition of the fluid domain is that the velocity is known. Turbulence intensity (I) and length scale of turbulent flow (l) are selected the characteristic parameters of the turbulent flow. Turbulence intensity (I) is calculated by the formula (13), and the length of the turbulent length scale (l) is expressed in the formula (15). Secondly, free flow is

used in fluid outlet condition. Thirdly, the free surface condition is treated by the symmetrical surface, which is the free slip surface. Finally, wall condition is defined as no slip boundary, the wall surface is uniform and the roughness height is equal to 0.25 mm

$$I \equiv \frac{u}{u_m} \cong \frac{4}{25} R_e^{-0.125} \tag{13}$$

$$R_e = 4\frac{u_m \mu}{H} \tag{14}$$

where μ is coefficient of kinematic viscosity, u_m is mean velocity in section, H stands for the depth of debris flow.

$$l = \frac{2}{5}\delta \tag{15}$$

In Eq. (15) δ is the thickness of boundary layer. In this study, the thickness of turbulent boundary layer is equal to $0.6H$.

2.4.2 Boundary Conditions of Solid Field

There are two kinds of boundary conditions for stress field that the first boundary condition (the surface forces of the solid filed are known) and the second boundary condition (the surface displacements of the solid filed are known). Boundary conditions of the check dam are most the second, which can be expressed as follow:

$$v_{ij} n_j = F_i(x, y, z) \tag{16}$$

where $n_{\tau\tau}$ is the directional derivative of the boundary and $\tau\tau_i$ ($\tau\tau$, $\tau\tau$, $\tau\tau$) is the surface displacement distribution function.

3 Numerical Model and Calculation Parameter Settings

3.1 Numerical Model

The numerical model mainly consists of the following two components: a drainage channel and a check dam. The numerical simulation is conducted in a 4-m-long open-water channel with a rectangular cross section of 0.4 × 0.4 m (width × height). The upper portion of the dam section is 0.2 m, the underside is 0.34 m, the dam height is 0.35 m, and the dam length is 0.4 m. The slope of the front of the dam is 1:0.3, while the slope behind the dam is 1:0; the width and height of the overflow mouth are 0.2 m and 0.05 m, respectively. The check dam is made of concrete. Figure 1 shows the three-dimensional diagram of the numerical model. Figure 2 shows the location diagram of representative points. Tetrahedral meshes were used in both fluid domain and solid domain. Figures 3 and 4 show the calculation model and mesh generation of fluid domain and solid domain. Rheological characteristic of debris flow is the relationship between the shear stress and the rheological velocity gradient of fluid flow. Currently, according to the theoretical derivation and the experimental simulation, a lot of rheological models have been proposed. The most common and general rheological models are as follows: Newtonian fluid model, Bingham fluid model, Pseudo plastic fluid model, Expansion body model, Yield pseudo plastic fluid model and Yield expansion body, et al. The relation curves between shear stress and velocity gradient of various fluid rheological models are shown in Fig. 5. A large number of test results show that Bingham rheological model is simple and easy to operate, and is consonant with the actual situation. Bingham fluid model is expressed in the formula (3).

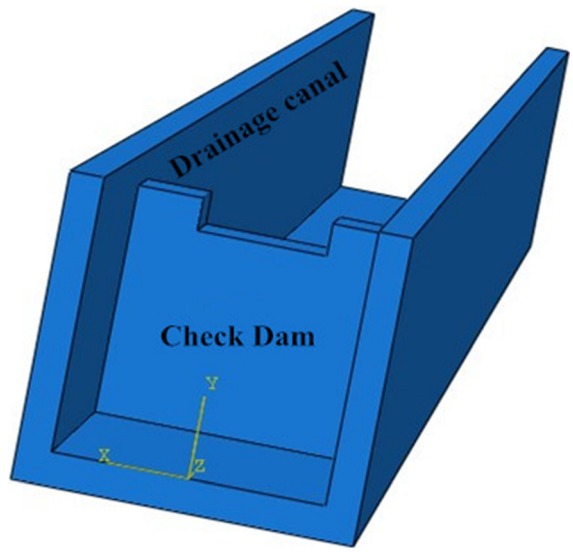

Fig. 1 Schematic diagram of the 3D model of check dam and drainage channel

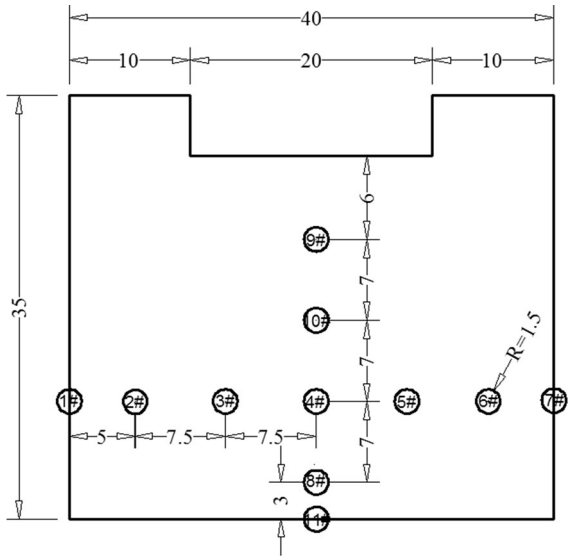

Fig. 2 Schematic diagram of the plane position of the key points (cm)

3.2 Calculation Parameters

According to the characteristics of numerical calculation software selected, the debris flow is simplified without considering solid particle sizes of the debris flow, but the density and characteristic parameters of fluid are kept consistent with the debris flow. To make use of the Bingham model formula, calculation formula of yield stress and stiffness coefficient should be known. Calculation formulas of yield stress and stiffness coefficient of debris flow were summarized based on experiments (Wu et al. 1993; Fei and Shu 2004; Kang et al. 2004). In this paper, Fei Xiangjun formulas (17, 18) were chosen. Moreover, according to the reference (Zeng 2014), yield strength and rigidity coefficient with different densities are given, which are shown in Table 1. Concrete check dam is regarded as elastomer, without considering the plastic. Mechanical parameters of concrete material are given in Table 2.

$$\eta = \eta_0 \left(1 - k\frac{S_{vf}}{S_{vm}}\right)^{-2.5} \left(1 - \frac{S_{vc}}{S'_{vm}}\right)^{-2.5} \tag{17}$$

$$\tau = 0.098 \exp\left(8.45\frac{S_v - S_{v0}}{S_{vm}} + 1.5\right) \tag{18}$$

where μ is the viscosity coefficient of debris flow, τ is the yield stress of debris flow, μ_0 is the viscosity coefficient of water, k is the concentration correction coefficient, S_{vf} is the pulp concentration without adding coarse particles, S_{vc} is the coarse particle concentration, S_{vm} and S'_{vm} respectively stand for the limit concentration without or with adding coarse particles, which are shown in the formula (20), S_{v0} is the critical concentration when suspension changes Newton fluid to Bingham fluid, which is expressed as follow:

$$S_{v0} = 1.26S_{vm}^{3.2} \tag{19}$$

$$S_{vm} = 0.92 - 0.2\lg\sum\frac{p_i}{d_i} \tag{20}$$

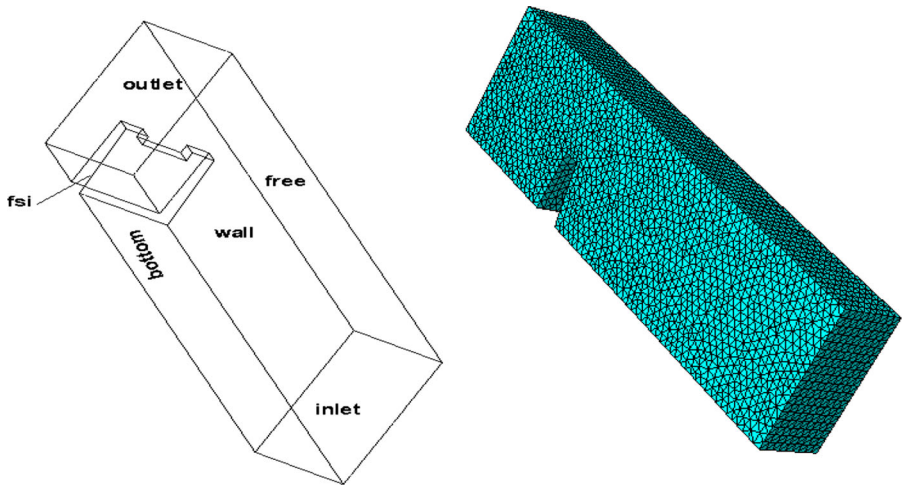

Fig. 3 Three dimensional computational model and mesh generation of fluid domain

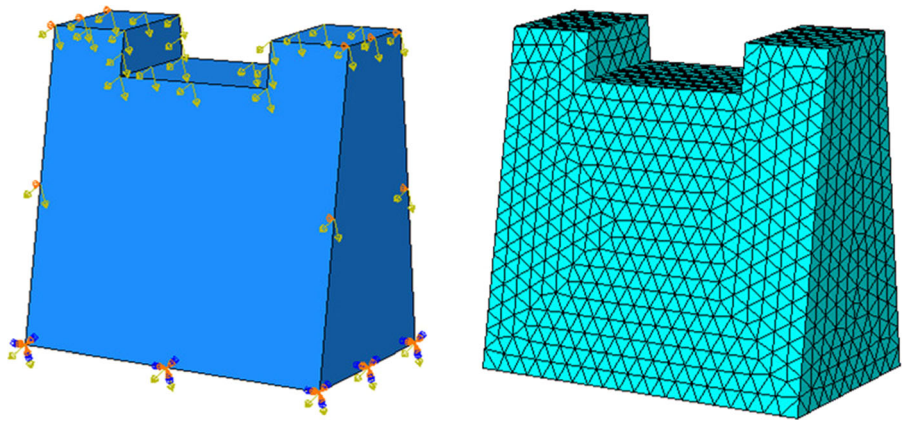

Fig. 4 Three dimensional computational model and mesh generation of solid domain

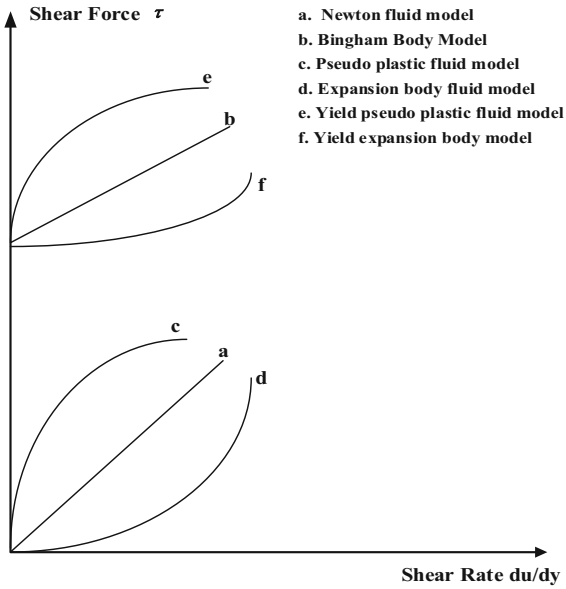

Fig. 5 Several rheological model

where d_i and p_i respectively stand for the average diameter and the corresponding weight percentage of the particle size group of the slurry particle size distribution.

3.3 Boundary Conditions

The inlet velocity is equal to 5 m/s, the depth of the inlet is equal to 8 cm, and other boundary conditions of fluid field are shown in the Sect. 2.4.1.

The bottom of the check dam completely fixed. Displacement of x direction of the check dam abutment is equal to 0, and other directions are free. What is more, other surfaces of the check dam are free completely.

Table 1 Debris flow physical and mechanical parameters

Bulk density of debris flow (kN/m^3)	14.20	15.50	18.10	19.50	10.00 (water)
Yield stress (Pa)	0.276	0.511	3.936	11.450	0
Stiffness constant (Pa s)	0.0042	0.0066	0.018	0.037	0.0010

Table 2 Concrete check dam mechanical parameters

Material	Density (kg/m^3)	Elastic modulus (GPa)	Poisson ratio	Tensile strength (MPa)
Concrete	2400	25.5	0.20	1.43

3.4 Set Analysis Steps

The two modules of computational fluid dynamics (CFD) and computational structural dynamics (CSD) use the same analysis settings, which are both transient analysis. And the number of steps is set to 200, with each analysis step time is 0.025 s.

3.5 Design Cases

At the initial moment of numerical calculation, the whole fluid field is filled with the air, which is an empty reservoir. Based on the experimental model, taking into account three factors like drainage groove slope, gradient of check dam upstream surface and bulk density of debris flow, the interaction between check dam and debris flow is carried out to simulate. Drainage groove slope is named A, gradient of check dam upstream surface is named B and bulk density of debris flow is named C, so the experimental conditions can be written $A_iB_jC_k$ (i = 1, 2, 3; j = 1, 2, 3; k = 1, 2, 3, 4, 5). Of those, i is equal to 1, 2 and 3 respectively stands for drainage groove slope being 9°, 12°, and 15°; j is equal to 1, 2 and 3 respectively stands for gradient of check dam upstream surface being 1:0, 1:0.15, 1:0.30 and j is equal to 1, 2,3 4, and 5 respectively stands for bulk density of debris flow (water) being 10 kN/m^3, 14.2 kN/m^3, 15.5 kN/m^3, 18.1 kN/m^3, 19.5 kN/m^3. There are 45-group simulation conditions, which are shown in Table 3.

4 Analysis of Debris Flow Field

Debris flow velocity and dynamic pressure are two important dynamic parameters in flow field, which are decisive factors in structure design of check dams. Distributions of debris flow velocity, dynamic pressure, static pressure and total pressure are studied in this paper.

4.1 Dynamic Variation of Flow Velocity of Debris Flow

In numerical calculation by the computational fluid dynamics software Fluent 14.0, the surface of check dams is taken as a coupled boundary, which is set for wall boundary. It is known that the velocity of wall boundary is always equal to zero in the calculation process by Fluent 14.0. Because of this, debris flow

Table 3 Design cases of numerical simulation

A Drainage channel slope (°)	*B* The dam upstream slope	*C* Bulk density of debris flow (water) (kN/m^3)	*A* Drainage channel slope (°)	*B* The dam upstream slope	*C* Bulk density of debris flow (water) (kN/m^3)	*A* Drainage channel slope (°)	*B* The dam upstream slope	*C* Bulk density of debris flow (water) (kN/m^3)
9	1:0	10.0	12	1:0	10.0	15	1:0	10.0
		14.2			14.2			14.2
		15.5			15.5			15.5
		18.1			18.1			18.1
		19.5			19.5			19.5
	1:0.15	10.0		1:0.15	10.0		1:0.15	10.0
		14.2			14.2			14.2
		15.5			15.5			15.5
		18.1			18.1			18.1
		19.5			19.5			19.5
	1:0.3	10.0		1:0.3	10.0		1:0.3	10.0
		14.2			14.2			14.2
		15.5			15.5			15.5
		18.1			18.1			18.1
		19.5			19.5			19.5

field nearby the check dam surface (being about 0.2 m (left) and 0.4 m (right) before the check dam) is selected as the research object of debris flow velocity. Taking $A_2B_3C_4$ as an example, the distributions of debris flow velocity for different time are shown in Fig. 6.

As shown in the Fig. 6, due to the blocking effect of check dams, some debris flow will stop before the dam with debris flow flowing to the check dam, which leads to debris flow velocity decreasing. It is also found that the flow rate of the bottom is greater than the top.

4.2 Pressure Distributions of Flow Field

There are three different types of pressure, i.e. static pressure, dynamic pressure and total pressure. Moreover, total pressure is the sum of dynamic pressure and static pressure. Taking the working condition of $A_2B_3C_4$ as an example, the distributions of static pressure, dynamic pressure and total pressure are analyzed. The distribution nephograms of static pressure, dynamic pressure and total pressure are given in the Figs. 7, 8 and 9.

As shown in the Fig. 7, because of debris flow piling up in the upstream face of check dam, hydrostatic pressure of the upstream face of check dam has an increasing trend with time from 1.5 s to 5.0 s. In the Fig. 8, it can be found that when the time is equal to 1.5 s, hydrodynamic pressure of the upstream face of check dam has the maximum value, and it has the minimum value when the time is equal to 5.0 s. Changes of total pressure with time has the same trend with the hydrodynamic pressure, which are shown in the Fig. 9.

4.3 The Variation Laws of Total Pressure of the Key Points on the Surface of Check Dam

The impact load is calculated between an initial data point (the first not equal to 0) and a terminal data point (the last data point of numerical simulation). The influencing factors mainly include the slope of the drainage channel, the gradient of check dam upstream surface and the unit density of debris flow. According to key point arrangement on the upstream face of check dam, the key points of 1#, 2#, 3#, 4#, 8#, 9#, 10# and 11# are selected as an example, and mean values of debris flow total pressure with different conditions are shown in Table 5.

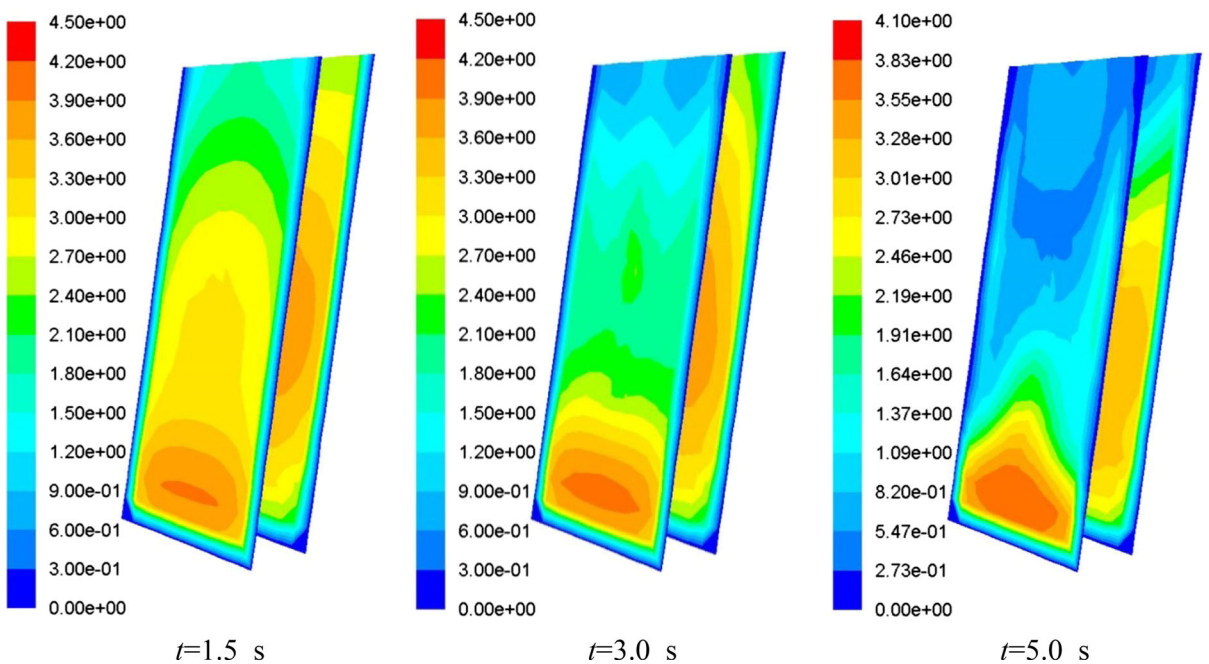

Fig. 6 Distributions of debris flow velocity for different time (m/s)

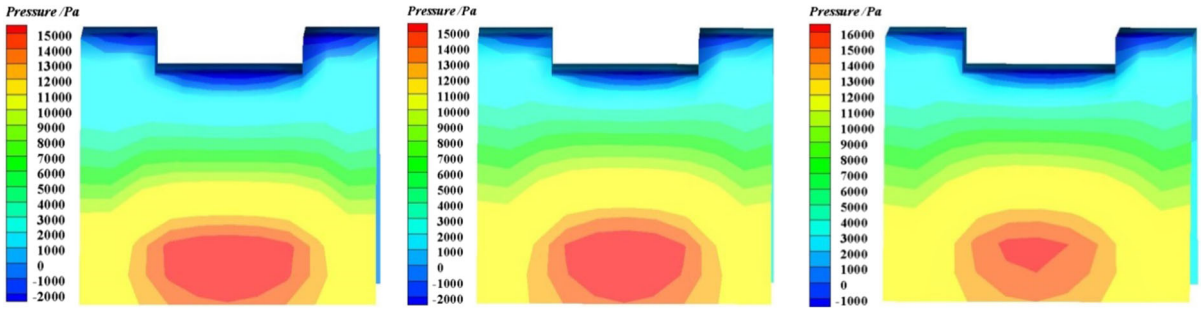

Fig. 7 Static pressure distributions on the check dam surface with different time

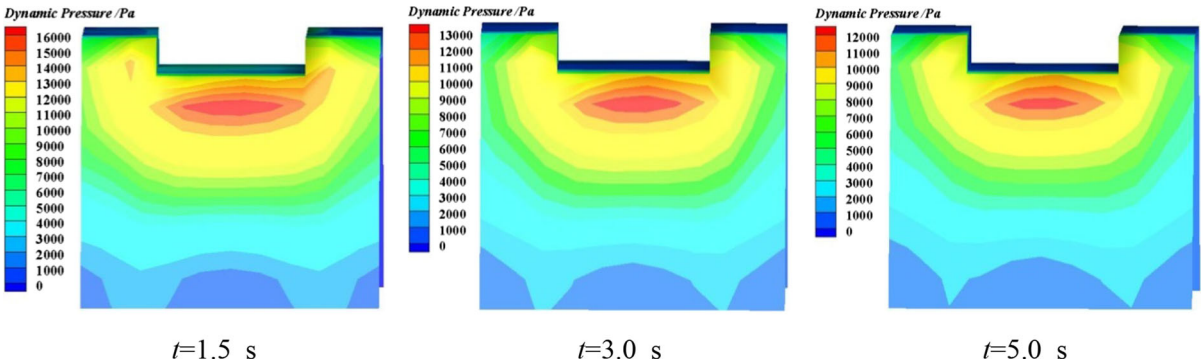

Fig. 8 Dynamic pressure distributions on the check dam surface with different time

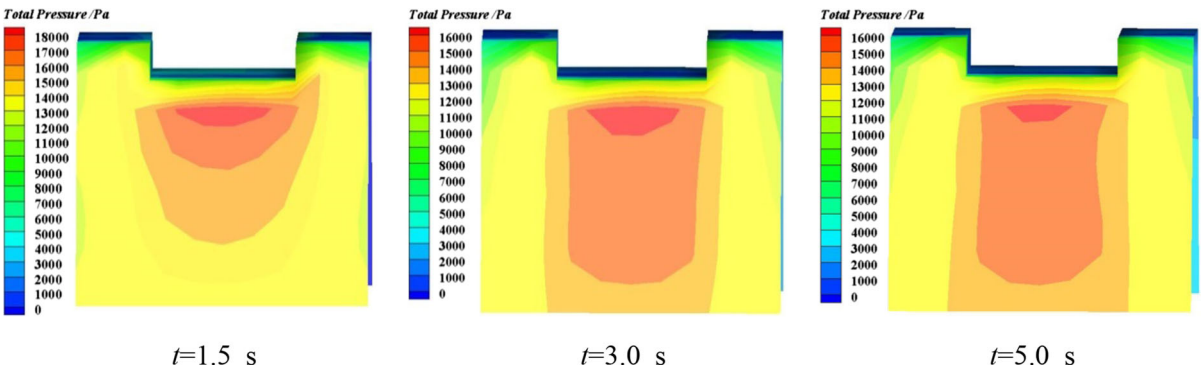

Fig. 9 Total pressure distributions on the check dam surface with different time

4.3.1 Single Factor Fitting

Through the analysis and solution of the calculation results in Table 4, it can be found that the fitting relationship between total pressure mean values and unit density of debris flow is a linear relationship with the other conditions remain unchanged, which can be expressed as follows:

$$P_1 = K_1\gamma + K_2 \tag{21}$$

where P_1 is total pressure mean values of debris flow, K_1 is scaling factor, K_2 is constant term, γ is unit density of debris flow or water.

The data of debris flow total pressure by changing unit density of debris flow, in Table 4, are introduced into the fitting formula (21). Adjusted R_1- square is less than 0.96, which has a high fitting degree.

Similarly, the above method can be applied to analyze the relationship between mean values of debris flow total pressure and drainage channel slope or the relationship between total pressure of debris flow and the gradient of check dam upstream surface. The fitted formulas can be expressed as follows:

$$P_2 = K_3 I + K_4 \tag{22}$$

$$P_3 = K_5 m + K_6 \tag{23}$$

where both P_2 and P_3 stand for mean values of debris flow total pressure, both K_4 and K_6 stand for scaling factors, I is the slope of drainage channel, 1/m is the gradient of check dam upstream surface. Adjusted R_2-square and R_2-square are respective less than 0.87, 0.80 (except for $A_3B_{(1\sim3)}C_1$), which have a quite high degree of fitting.

4.3.2 Multiple Factors Fitting

According to the results of single factor fitting and the reference (He 2014), multiple factor analysis is carried out to fit the relationship between mean values total pressure and the three factors, i.e. drainage groove slope, unit density of debris flow and the gradient of check dam upstream surface. Mean values of debris flow total pressure is taken as dependent variable, named as P, and drainage groove slope, unit density of debris flow and the gradient of check dam upstream surface are all taken as independent variables, named as I, γ, m. The data of the dependent variable and independent variable is shown in Table 5. The linear multivariate fitting is carried out by the software MATLAB, the expression of which is given as follows:

$$P = a_1\gamma + a_2 I + a_3 m + b \tag{24}$$

where all a_1,a_2,a_3 and b stand for fitting coefficients.

Fitting coefficients of the formula (24) about the key points (1#, 3#, 8# and 11#) are obtained by calling the function of MATLAB data processing platform, which are written on Matrix form as follows:

$$A = \begin{bmatrix} 0.614, 0.191, -2.313, -2.133 \\ 0.786, 0.314, -0.786, -3.859 \\ 0.750, 0.291, -1.351, -3.501 \\ 0.719, 0.273, -1.387, -3.13 \end{bmatrix} \tag{25}$$

So the formula (24) can be expressed as follows:

$$P = A \begin{bmatrix} \gamma \\ I \\ m \\ 1 \end{bmatrix} = \begin{bmatrix} 0.614, 0.191, -2.313, -2.706 \\ 0.786, 0.315, -0.948, -4.806 \\ 0.750, 0.291, -0.948, -4.373 \\ 0.719, 0.273, -1.387, -3.947 \end{bmatrix} \begin{bmatrix} \gamma \\ I \\ m \\ 1 \end{bmatrix} \tag{26}$$

Adjusted $R_{1\#}$-square, $R_{3\#}$-square, $R_{8\#}$-square, $R_{11\#}$-square are less than 0.9935, 0.9927, 0.9938 and 0.9957, respectively. And variances of root-mean-square error are equal to 0.1713, 0.2358, 0.2059 and 0.1642, respectively. The comparison between fitted values and values of numerical simulation (measured values) is shown in the Fig. 10.

5 Dynamic Response of Check Dam under the Impact Effect of Debris Flow

Debris flow impact force can cause the check dam deformation and even damage, which has a bad influence on the normal operation of the dam. The changes of the external factors (such as the slope of drainage channel, the unit density of debris flow, etc.) can make the impact force of the debris flow change, which cause stress field of the check dam to be changed. Taking the 45-group test conditions in Table 3 for example, the tendency of stress field dynamic variation is studied.

5.1 The Dynamic Evolution Laws of Mises Equivalent Stress and Maximum Tensile Stress with Time

Schematic diagram of the plane distribution of the key points of the check dam upstream surface is shown in the Fig. 11. Taking the lateral points such as 1#, 3#, 6#, 9# and 11# for example, the dynamic evolution laws of Mises equivalent stress and maximum tensile stress with time for the above five points are shown in the Fig. 12a, b. Also, taking the vertical points in the Fig. 11 for example, the dynamic evolution laws of Mises equivalent stress and maximum tensile stress with time for the above five points are shown in the Fig. 12c, d.

Table 4 Total pressure mean value of the critical points on the check dam surface under different conditions

Key points different conditions	1# (Pa)	2# (Pa)	3# (Pa)	4# (Pa)	8# (Pa)	9# (Pa)	10# (Pa)	11# (Pa)
$A_1B_1C_1$	5747.2	6165.4	7225.7	7268.8	6885.1	8097.0	7058.2	6704.8
$A_1B_1C_2$	8176.9	8760.5	10,183.2	10,337.4	9774.1	11,547.4	11,060.3	9506.1
$A_1B_1C_3$	8930.5	9565.0	11,135.6	11,279.9	10,660.7	12,423.0	10,954.8	10,375.2
$A_1B_1C_4$	10,469.7	11,314.8	13,196.6	13,219.8	12,488.7	14,516.2	12,888.4	12,172.0
$A_1B_1C_5$	11,299.1	12,101.1	14,090.1	14,250.3	13,463.7	15,813.8	13,922.1	13,143.6
$A_1B_2C_1$	5616.3	6048.8	7103.2	7201.9	6777.1	7886.0	6964.2	6601.4
$A_1B_2C_2$	8001.3	8650.4	10,095.1	10,248.5	9612.0	11,241.9	9923.7	9413.1
$A_1B_2C_3$	8736.0	9449.9	11,014.2	10,925.5	10,491.8	12,276.9	10,847.3	10,276.5
$A_1B_2C_4$	10,223.5	11,221.5	12,905.5	13,015.7	12,315.2	14,381.3	12,755.1	12,057.4
$A_1B_2C_5$	11,011.6	12,047.5	13,895.2	13,942.1	13293.3	15,548.2	13,780.8	13,012.8
$A_1B_3C_1$	5450.4	5924.4	7014.7	6897.7	6645.8	7735.7	6751.9	6441.0
$A_1B_3C_2$	7754.6	8560.3	9979.5	9804.7	9433.7	11,026.8	9717.8	9138.2
$A_1B_3C_3$	8509.1	8812.2	9995.0	10,709.3	9828.1	12,053.7	10,773.1	10,022.1
$A_1B_3C_4$	10,043.5	11,085.1	12,850.9	12,583.1	12,125.0	14,161.6	12,555.2	11,726.2
$A_1B_3C_5$	10,839.1	12,059.1	13,842.9	13,579.3	13,057.2	15,335.0	13,457.5	12,627.5
$A_2B_1C_1$	6239.3	6740.7	7705.6	7825.9	7513.5	8850.1	8315.4	7338.2
$A_2B_1C_2$	8905.3	9612.5	10,973.2	11,146.9	10,692.4	12,580.2	11,822.8	10,443.6
$A_2B_1C_3$	9869.0	10,650.3	12,153.8	12,346.2	11,841.2	13,728.1	12,904.7	11,266.8
$A_2B_1C_4$	11,528.0	12,442.2	14,195.5	14,415.0	13,822.9	16,007.3	15,072.7	13,103.1
$A_2B_1C_5$	12,422.6	13,404.8	15,282.5	15,527.1	14,897.4	17,334.7	16,298.6	14,160.6
$A_2B_2C_1$	5821.4	6223.7	7288.4	7448.1	7281.5	8567.0	8175.8	7210.8
$A_2B_2C_2$	8454.7	9342.6	10,931.0	11,068.5	10,517.3	12,327.2	11,677.0	10,198.9
$A_2B_2C_3$	9234.6	10,202.3	11,936.8	12,199.3	11,483.2	13,548.1	12,756.8	11,135.1
$A_2B_2C_4$	10,796.8	11,931.8	13,957.9	14,271.9	13,423.9	15,816.0	14,934.3	13,017.8
$A_2B_2C_5$	11,642.1	12,865.0	15,049.3	15,400.9	14,489.2	17,099.7	16,138.3	14,058.4
$A_2B_3C_1$	5627.6	6412.7	7724.7	7907.7	7023.5	8223.1	7919.7	7036.0
$A_2B_3C_2$	8284.4	9117.6	10,973.3	10,942.9	10,334.7	12,147.7	11,444.3	9984.1
$A_2B_3C_3$	9045.0	9953.6	11,978.3	12,074.6	11,279.0	13,386.7	12,480.8	10,896.2
$A_2B_3C_4$	10,561.6	11,626.7	14,001.1	14,157.5	13,184.8	15,670.3	14,719.1	12,736.3
$A_2B_3C_5$	11,387.6	12,537.9	15,102.9	15,309.8	14,247.6	16,971.5	15,886.5	13,773.3
$A_3B_1C_1$	6676.7	7277.0	8413.8	8538.8	7947.2	9510.5	8910.3	7747.1
$A_3B_1C_2$	9529.3	10,386.8	12,005.4	12,175.9	11,319.5	13,621.9	12,683.9	11,118.9
$A_3B_1C_3$	10,377.3	11,303.0	13,045.1	13,254.5	12,319.0	14,773.8	13,859.8	12,119.2
$A_3B_1C_4$	12,136.4	13,221.1	15,260.6	15,508.0	14,402.8	17,293.2	16,245.9	14,103.4
$A_3B_1C_5$	13,080.8	14,245.1	16,438.6	16,708.8	15,536.0	18,658.0	17,543.2	15,237.0
$A_3B_2C_1$	6220.4	6916.7	8286.2	8380.3	7835.7	9341.5	8823.0	7631.0
$A_3B_2C_2$	8947.0	9943.4	11,756.6	12,032.1	11,235.1	13,416.1	12,582.5	10,942.1
$A_3B_2C_3$	9771.5	10,858.7	12,839.5	13,140.9	12,266.3	14,649.5	13,755.8	11,946.1
$A_3B_2C_4$	11,429.4	12,703.8	15,023.9	15,385.5	14,350.2	17,138.5	16,128.3	13,974.2
$A_3B_2C_5$	12,317.6	13,693.8	16,197.0	16,594.1	15,479.3	18,505.6	17,413.3	15,077.4
$A_3B_3C_1$	6122.9	6939.4	8112.8	8345.7	7710.4	9159.8	8617.1	7489.2
$A_3B_3C_2$	8716.0	9871.7	11,672.9	12,010.5	11,083.5	13,309.1	12,313.4	10,624.4
$A_3B_3C_3$	9520.5	10,782.3	12,751.7	13,122.6	12,101.9	14,536.8	13,510.4	11,598.0
$A_3B_3C_4$	11,139.3	12,623.9	14,934.3	15,369.5	14,154.7	17,018.5	15,951.6	13,563.0
$A_3B_3C_5$	12,004.4	13,602.3	16,104.8	16,590.1	15,276.8	18,374.0	17,302.4	14,638.8

Table 5 Data of fitting dependent variables and independent variables

Cases	$A_1B_1C_1$	$A_1B_1C_2$	$A_1B_1C_3$	$A_1B_1C_4$	$A_1B_1C_5$	$A_1B_2C_1$	$A_1B_2C_2$	$A_1B_2C_3$	$A_1B_2C_4$	$A_1B_2C_5$
I	9	9	9	9	9	9	9	9	9	9
m	0	0	0	0	0	0.15	0.15	0.15	0.15	0.15
γ	10.0	14.2	15.5	18.1	19.5	10.0	14.2	15.5	18.1	19.5
$P_{1\#}$ (kPa)	5.75	8.18	8.93	10.47	11.30	5.62	8.00	8.74	10.22	11.01
$P_{3\#}$ (kPa)	7.23	10.18	11.14	13.20	14.09	7.10	10.10	11.01	12.91	13.90
$P_{8\#}$ (kPa)	6.89	9.77	10.66	12.49	13.46	6.78	9.61	10.49	12.32	13.29
$P_{11\#}$ (kPa)	6.70	9.51	10.38	12.17	13.14	6.60	9.41	10.28	12.06	13.01
Cases	$A_1B_3C_1$	$A_1B_3C_2$	$A_1B_3C_3$	$A_1B_3C_4$	$A_1B_3C_5$	$A_2B_1C_1$	$A_2B_1C_2$	$A_2B_1C_3$	$A_2B_1C_4$	$A_2B_1C_5$
I	9	9	9	9	9	12	12	12	12	12
m	0.3	0.3	0.3	0.3	0.3	0	0	0	0	0
γ	10.0	14.2	15.5	18.1	19.5	10.0	14.2	15.5	18.1	19.5
$P_{1\#}$ (kPa)	5.45	7.75	8.51	10.04	10.84	6.24	8.91	9.87	11.53	12.42
$P_{3\#}$ (kPa)	7.01	9.98	10.00	12.85	13.84	7.71	10.97	12.15	14.20	15.28
$P_{8\#}$ (kPa)	6.65	9.43	9.83	12.13	13.06	7.51	10.69	11.84	13.82	14.90
$P_{11\#}$ (kPa)	6.44	9.14	10.02	11.73	12.63	7.34	10.44	11.27	13.10	14.16
Cases	$A_2B_2C_1$	$A_2B_2C_2$	$A_2B_2C_3$	$A_2B_2C_4$	$A_2B_2C_5$	$A_2B_3C_1$	$A_2B_3C_2$	$A_2B_3C_3$	$A_2B_3C_4$	$A_2B_3C_5$
I	12	12	12	12	12	12	12	12	12	12
m	0.15	0.15	0.15	0.15	0.15	0.3	0.3	0.3	0.3	0.3
γ	10.0	14.2	15.5	18.1	19.5	10.0	14.2	15.5	18.1	19.5
$P_{1\#}$ (kPa)	5.82	8.45	9.23	10.80	11.64	5.63	8.28	9.05	10.56	11.39
$P_{3\#}$ (kPa)	7.29	10.93	11.94	13.96	15.05	7.72	10.97	11.98	14.00	15.10
$P_{8\#}$ (kPa)	7.28	10.52	11.48	13.42	14.49	7.02	10.33	11.28	13.18	14.25
$P_{11\#}$ (kPa)	7.21	10.20	11.14	13.02	14.06	7.04	9.98	10.90	12.74	13.77
Cases	$A_3B_1C_1$	$A_3B_1C_2$	$A_3B_1C_3$	$A_3B_1C_4$	$A_3B_1C_5$	$A_3B_2C_1$	$A_3B_2C_2$	$A_3B_2C_3$	$A_3B_2C_4$	$A_3B_2C_5$
I	15	15	15	15	15	15	15	15	15	15
m	0	0	0	0	0	0.15	0.15	0.15	0.15	0.15
γ	10.0	14.2	15.5	18.1	19.5	10.0	14.2	15.5	18.1	19.5
$P_{1\#}$ (kPa)	6.68	9.53	10.38	12.14	13.08	6.22	8.95	9.77	11.43	12.32
$P_{3\#}$ (kPa)	8.41	12.01	13.05	15.26	16.44	8.29	11.76	12.84	15.02	16.20
$P_{8\#}$ (kPa)	7.95	11.32	12.32	14.40	15.54	7.84	11.24	12.27	14.35	15.48
$P_{11\#}$ (kPa)	7.75	11.12	12.12	14.10	15.24	7.63	10.94	11.95	13.97	15.08
Cases		$A_2B_3C_1$		$A_2B_3C_2$		$A_2B_3C_3$		$A_2B_3C_4$		$A_2B_3C_5$
I		15		15		15		15		15
m		0.3		0.3		0.3		0.3		0.3
γ		10.0		14.2		15.5		18.1		19.5
$P_{1\#}$ (kPa)		6.12		8.72		9.52		11.14		12.00
$P_{3\#}$ (kPa)		8.11		11.67		12.75		14.93		16.10
$P_{8\#}$ (kPa)		7.71		11.08		12.10		14.15		15.28
$P_{11\#}$ (kPa)		7.49		10.62		11.60		13.56		14.64

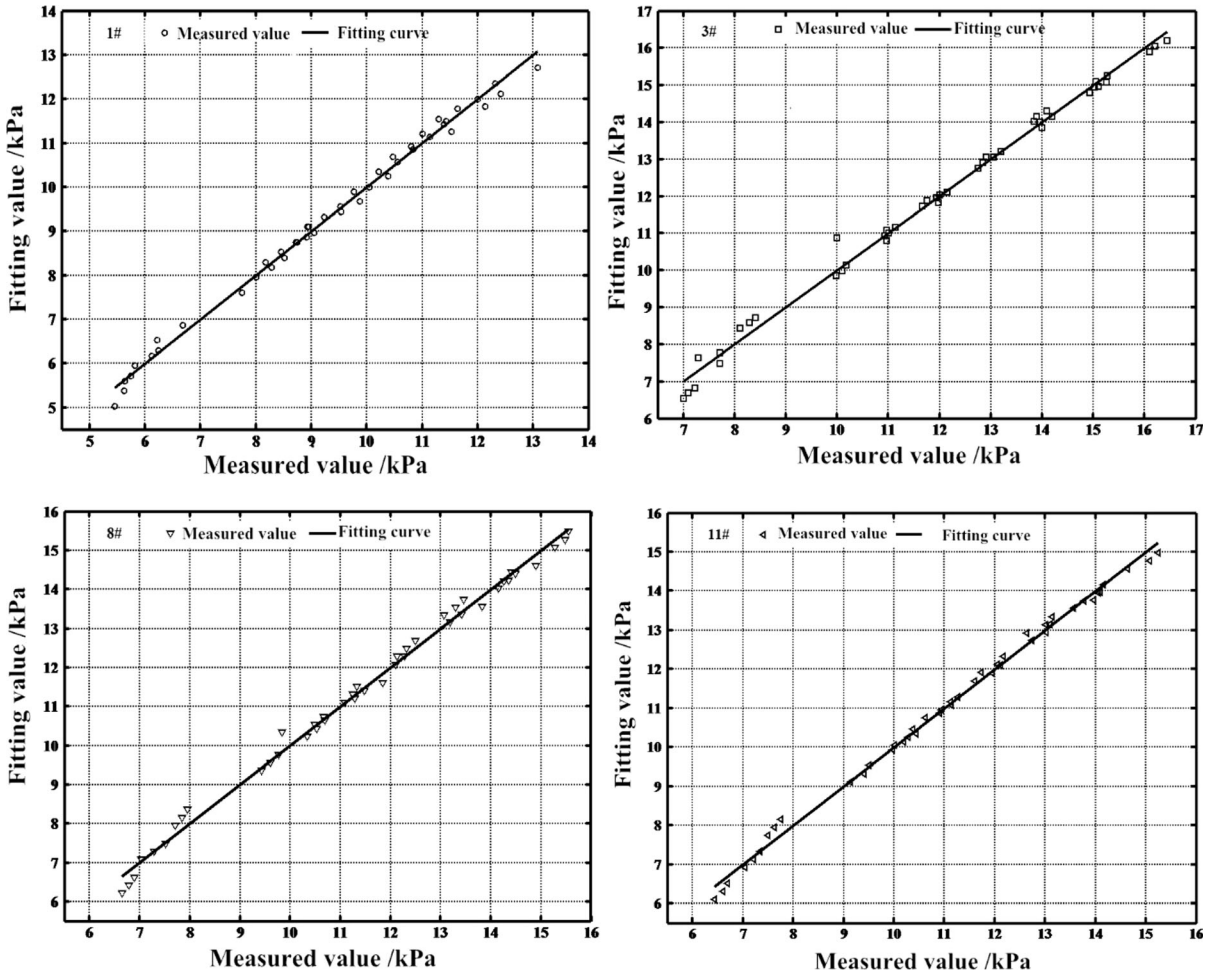

Fig. 10 Comparison between fitted values and measured values (values of numerical simulation)

Figure 12a–d shows Mises equivalent stress and maximum tensile stress first increase until maximum value then decrease to minimum value, finally remains at a certain level with the time increasing.

5.2 Distribution Trend of the Maximum Value of Mises Equivalent Stress and the Maximum Tensile Stress Along the Horizontal and Vertical of the Check Dam

In order to analyze distribution trend of the maximum values of Mises equivalent stress and the maximum tensile stress along the transverse and longitudinal direction of the check dam upstream surface, horizontal path (G–H in Fig. 11) and vertical path (M–N in Fig. 11) made of the nodes on the upstream surface of check dam are taken as the research object. Distribution trend of the maximum value of Mises equivalent stress and the maximum tensile stress of the nodes along the transverse and longitudinal direction (G-H, M–N) of the check dam upstream surface are mainly discussed, which are shown in the Figs. 13 and 14.

As shown in the Fig. 13, the maximum values of Mises equivalent stress and maximum tensile stress along horizontal direction of the check dam upstream surface are in a symmetrical distribution. Mises equivalent stress maximum values of nodes on the overflow outlet are greater than the values of nodes on the dam abutment. However, the maximum values of maximum tensile stress of nodes on the dam abutment are greater than the values of nodes on the overflow outlet.

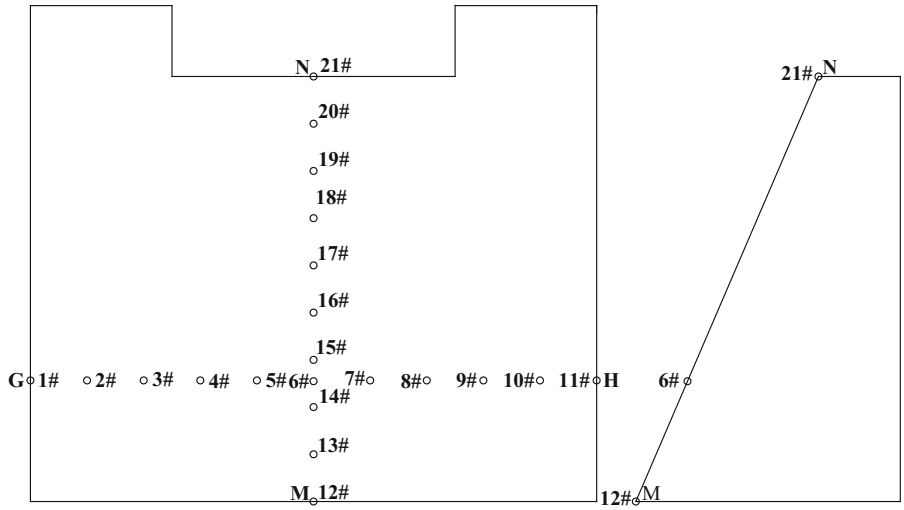

Fig. 11 Plane distribution schematic diagram of the key points

Figure 14 shows Mises equivalent stress maximum values of nodes along vertical direction have a trend of decrease with the increase of height, the node at the bottom having the maximum value. Nevertheless, the maximum values of maximum tensile stress of nodes along vertical direction first decrease then slightly increase with the increase of height.

5.3 Evolution Laws of Stress Field of the Check Dam with the Influence Factors

Taking Mises equivalent stress and the maximum tensile force as evaluation parameters, variation trends of the above two evaluation parameters with the changes of drainage groove slope, unit density of debris flow and the gradient of check dam upstream surface are studied

5.3.1 Evolution Laws of the Maximum Value of Mises Equivalent Stress and Maximum Tensile Stress with the Changes of the Drainage Channel Slope

Evolution laws of the maximum value of Mises equivalent stress and maximum tensile stress of nodes for the whole elements of the check dam with the changes of the drainage channel slope are shown in Figs. 15 and 16.

As shown in the Fig. 15, making other external conditions remain unchanged, the maximum value of Mises equivalent stress of nodes linearly increases with the increase of drainage groove slope for all different conditions. Through contrastively analyzing the vertical numerical values, it is also found that Mises equivalent stress has the maximum value under the condition of $A_{(1-3)}B_1C_5$ and has the minimum value for the condition of $A_{(1-3)}B_3C_1$. Figure 16 shows, keeping other factors remain unchanged, the maximum value of maximum tensile stress of nodes increases nonlinearly with the drainage groove slope increasing for all different conditions. Moreover, maximum tensile stress has the maximum value under the condition of $A_{(1-3)}B_1C_5$ and has the minimum value for the condition of $A_{(1-3)}B_3C_1$, which is the same as the maximum value of maximum tensile stress.

5.3.2 Evolution Laws of the Maximum Value of Mises Equivalent Stress and Maximum Tensile Stress with the Changes of Check Dam Upstream Surface Gradient

Evolution laws of the maximum value of Mises equivalent stress and maximum tensile stress of nodes for all the elements of the check dam with the changes of check dam upstream surface gradient are shown in the Figs. 17 and 18.

As shown in the Figs. 17 and 18, making other external conditions remain unchanged, the maximum value of Mises equivalent stress and maximum tensile

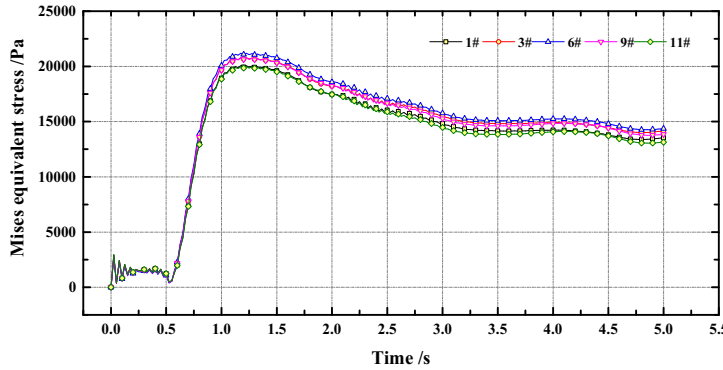

(a) Lateral points（Mises equivalent stress）

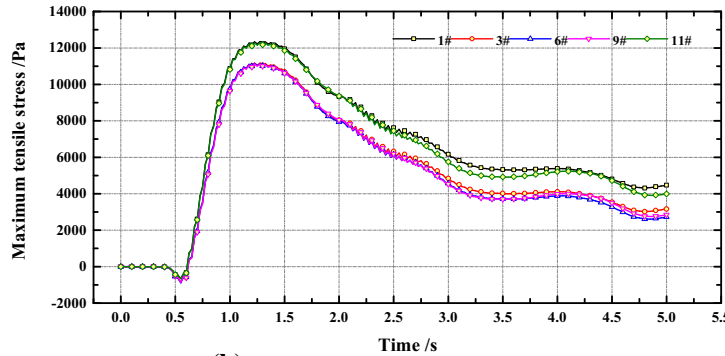

(b) Lateral points (maximum tensile stress)

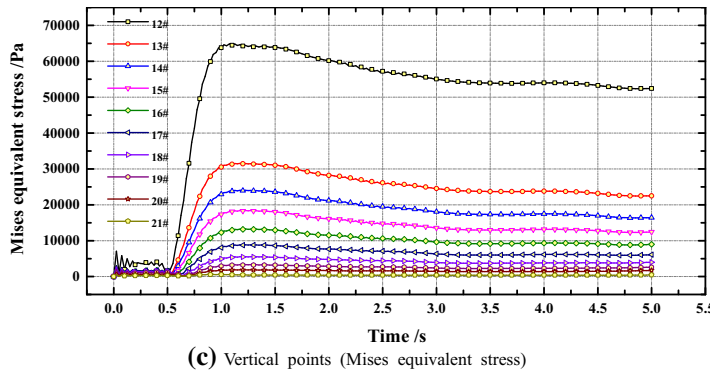

(c) Vertical points (Mises equivalent stress)

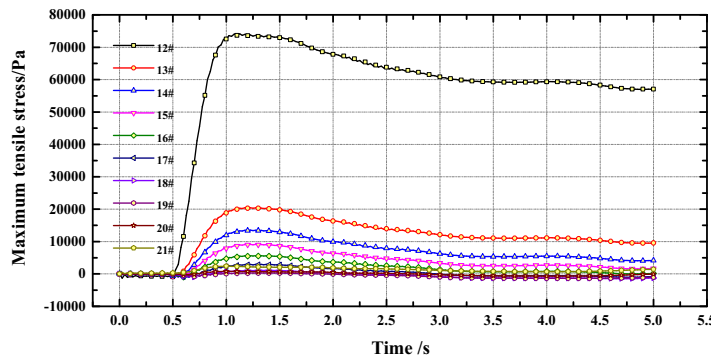

(d) Vertical points (maximum tensile stress)

Fig. 12 Dynamic evolution laws of Mises equivalent stress and maximum tensile stress with time of different nodes

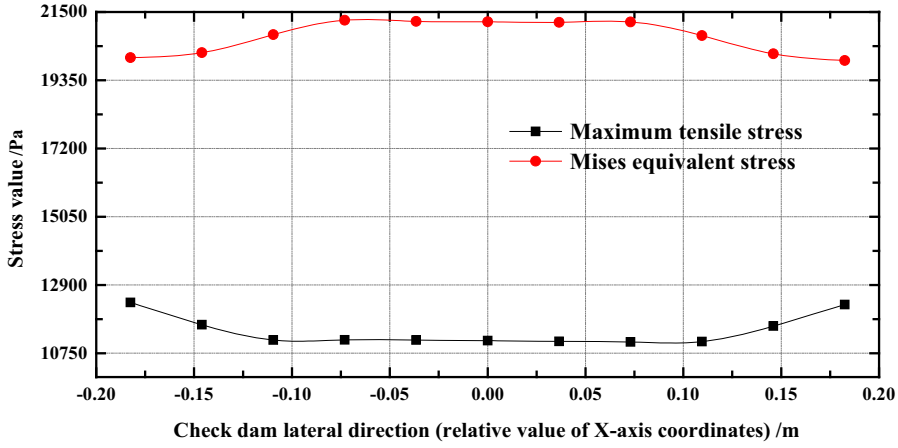

Fig. 13 Distribution trend of the maximum value of Mises equivalent stress and the maximum tensile stress along the transverse direction (G–H) of the check dam upstream surface

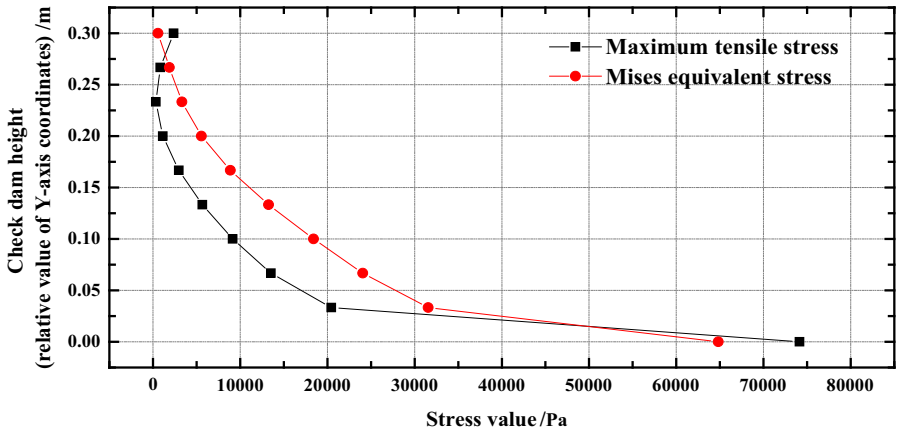

Fig. 14 Distribution trend of the maximum value of Mises equivalent stress and the maximum tensile stress along the longitudinal direction (M–N) of the check dam upstream surface

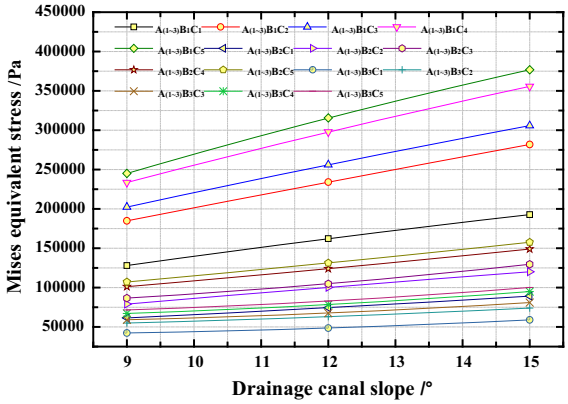

Fig. 15 Evolution laws of the Mises equivalent stress

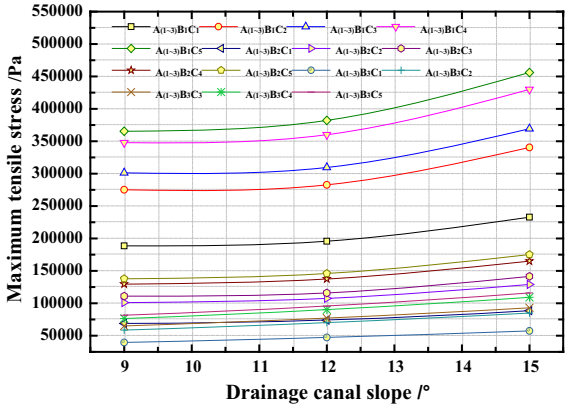

Fig. 16 Evolution laws of the maximum tensile stress

stress of nodes linearly decrease with the slower of check dam upstream surface gradient for all different conditions. Through contrastively analyzing the vertical numerical values, it is also found that Mises equivalent stress and maximum tensile stress of nodes have the maximum values under the condition of

$A_3B_{(1-3)}C_5$ and have the minimum values for the condition of $A_1B_{(1-3)}C_1$.

5.3.3 *Evolution Laws of the Maximum Value of Mises Equivalent Stress and Maximum Tensile Stress with the Changes of Unit Densities of Debris Flow*

Evolution laws of the maximum value of Mises equivalent stress and maximum tensile stress of nodes for all the elements of the check dam with the changes of debris flow unit density are shown in the Figs. 19 and 20.

As shown in the Figs. 19 and 20, making other external conditions remain unchanged, the maximum value of Mises equivalent stress and maximum tensile stress of nodes linearly increase with the increase of debris flow unit density for all different conditions. Through contrastively analyzing the vertical numerical values, it is also found that Mises equivalent stress and maximum tensile stress of nodes have the maximum values under the condition of $A_3B_1C_{(1-5)}$ and have the minimum values for the condition of $A_1B_3C_{(1-5)}$.

From Figs. 15, 16, 17, 18, 19 and 20, it can be found that Mises equivalent stress and maximum tensile stress of nodes for the whole elements of the check dam have the maximum value under the condition of $A_3B_1C_5$ and have the minimum value under the condition of $A_1B_3C_1$. There are significant positive correlations between the maximum value of Mises equivalent stress and maximum tensile stress and the drainage channel slope and debris flow unit density. Nevertheless, there is a significant negative correlation between the maximum value of Mises equivalent stress and maximum tensile stress and check dam upstream surface gradient. For the all 45 conditions,

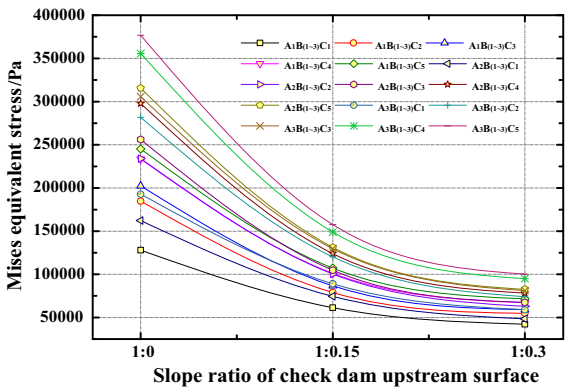

Fig. 17 Evolution laws of the Mises equivalent stress

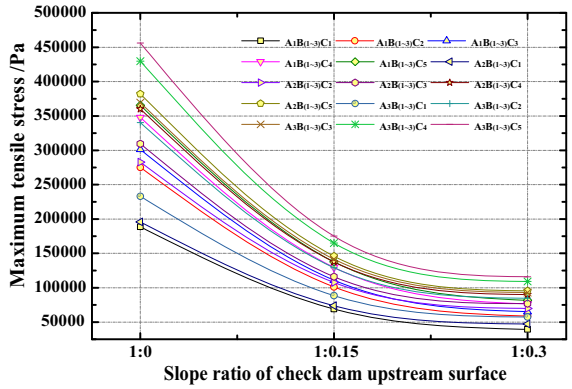

Fig. 18 Evolution laws of the maximum tensile stress

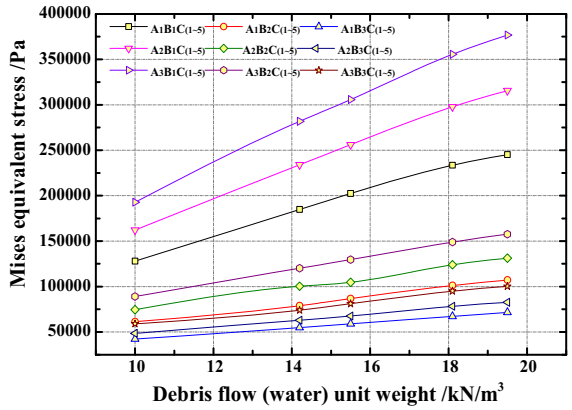

Fig. 19 Evolution laws of the Mises equivalent stress

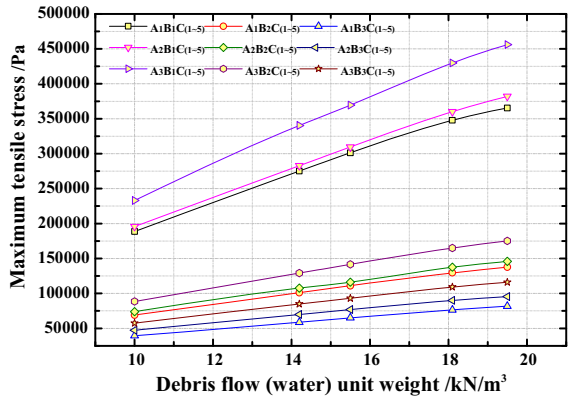

Fig. 20 Evolution laws of the maximum tensile stress

the maximum and minimum values of Mises equivalent stress are 376,794.1 Pa, 42,194.4 Pa, and the maximum is the minimum by 8.9 times. In addition, the maximum and minimum values of maximum tensile stress are 456,013.4 Pa, 39,548.1 Pa, and the maximum is the minimum by 11.5 times.

6 Conclusions

Based on the theory of fluid–solid coupling, the numerical model of the interaction between debris flow and sand-blocking dam is carried out based on the experimental model. The dynamic response of the check dam under the debris flow and the influence of the check dam on the debris flow field are obtained. The simulation results show the following:

1. The mean value of the impact force of the debris flow increases with the slope of the drainage channel and the weight of the debris flow, and decreases with the decrease of the slope ratio of the upstream surface of the sand dam, which is basically consistent with the reference (Yu et al. 2018).
2. The impact force of the debris flow at the observation point increases firstly to the maximum value, then decreases to the minimum value and remains constant, which have a similar trend with the Mises equivalent stress, the maximum tensile stress and the displacement in the stress field of the check dam.

Acknowledgements This study was supported by the Doctoral Scientific Research Foundation of Linyi University (Grant No. LYDX2016BS109); National Natural Science Foundation (Grant No. 51704152); National Key Technology R&D Program of the Ministry of Science and Technology (Grant No. 2014BAL05B01). Furthermore, we would like to thank the two anonymous reviewers and editors for their comments.

References

Armanini A, Scotton P (1993) On the dynamic impact of a debris flow on structures. In: Proceedings of the congress-international association for hydraulic research. Local Organizing Committee of the XXV Congress, vol 3, pp 203–210

Bathe KJ (2003) ADINA theory and modeling guide. ADINA R&D, Watertown

Bugnion L, McArdell BW, Bartelt P et al (2012a) Measurements of hillslope debris flow impact pressure on obstacles. Landslides 9(2):179–187

Bugnion L, Bötticher A, Wendeler C (2012b) Large scale field testing of hill slope debris flows resulting in the design of flexible protection barriers. In: Proceedings of 12th interpraevent Grenoble/France

Chen HK, Tang HM, Chen YY (2007) Highway Mud-rock Flow Mechanics. Science Press, Beijing

Chen HH, Tang HM, Ye SQ (2008) Study on mud–rock flows along high ways in China. Chin J Geol Hazard Control 19(1):1–5

Chen XS, Wang JL, Yi R (2013) Fluid–solid interaction dynamic response of masonry structures under debris flow action. Eur J Environ Civ Eng 17(9):841–859

Cui P (2009) Advances in mud-rock flow prevention in China. Sci Soil Water Conserv 7(5):7–13

Cui P, Zeng C, Lei Y (2015) Experimental analysis on the impact force of viscous debris flow. Earth Surf Proc Land 40:1644–1655

DeNatale JS, Iverson RM, Major JJ et al (1999) Experimental testing of flexible barriers for containment of debris flows. USGS Open-File Report 99-205. US Geological Survey

Fei XJ, Shu AP (2004) Movement mechanism and disaster control for debris flow. Tsinghua University Press, Beijing

He XX (2014) Experimental study on the shock characteristics of debris flow considering different slurry viscosity and gradation particles. Chongqing Jiaotong University

He XY, Tang HM, Zhu XZ et al (2013) Tests for impacting characteristics of mud-rock flow slurry. J Vib Shock 32(24):127–134

He XY, Tang HM, Chen HK (2014a) Experimental study on impacting characteristic of mud–rock flow considering different slurry viscosities, solid phase ratios and grain diameters. Chin J Geotech Eng 36(5):977–982

He XY, Chen HK, Tang HM et al (2014b) Experimental study on impacting characteristics of mud-rock flow heads. J Chongqing Jiaotong Univ (Nat Sci) 33(1):85–89. https://doi.org/10.3969/j.issn.1674-0696.2014.01.19 **(In Chinese, with English abstract)**

Hu KH, Wei FQ, Li Y (2011) Real-time measurement and preliminary analysis of debris-flow impact force at Jiangjia Ravine, China. Earth Surf Proc Land 36(9):1268–1278

Hübl J, Suda J, Proske D, Kaitna R, Scheidl C (2009) Debris flow impact estimation. In: Proceedings, international symposium on water management and hydraulic engineering, Ohrid/Macedonia, pp 137–148

Iverson RM, Matthew L, Lahusen RG et al (2010) The perfect debris flow? Aggregated results from 28 large-scale experiments. J Geophys Res Atmos 115(F3):438–454

Kang ZC, Li ZF, Ma GN et al (2004) The study on debris flow in China. Science Press, Beijing

König U (2006) Real scale debris flow tests in the Schesatobel-valley. Master's thesis, University of Natural Resources and Life Sciences, Vienna, Austria

Lei Y, Cui P, Zeng C et al (2018) An empirical mode decomposition-based signal process method for two-phase debris flow impact. Landslides 15:297–307

Leonardi A (2015) Numerical simulation of debris flow and interaction between flow and obstacle via DEM. University of Padova

Leonardi A, Wittel FK, Mendoza M et al (2015) Particle-fluid-structure interaction for debris flow impact on flexible barriers. Comput Aided Civ Infrastruct Eng 31(5):323–333

Li K, Tang HM, Yi LY et al (2008) Numerical simulation on coupling problem between Debris flow and bank of debris flow valley. J Chong qing Jian zhu Univ 30(1): 68–71+76

Liu RX, Shu QW (2003) Several new methods for computational fluid dynamics. Science Press, Beijing

Liu LJ, Wei H (1997) Study of impact of mud–rock flow. J Sichuan Univ (Eng Sci Ed) 1(2):99–102 **(In Chinese, with English abstract)**

Moriguchi S, Borja RI, Yashima A et al (2009) Estimating the impact force generated by granular flow on a rigid obstruction. Acta Geotech 4(1):57–71

Okuda S, Okunishi K (1980) Observation at Kamikamihori valley of Mt. Yakedake. Excursion guide-book the third meeting of JGU commission on field experiments in geomorphology, disaster prevention research institute Kyoto unit, Japan, pp 1–139

Scheidl C, Chiari M, Kaitna R et al (2013) Analysing debris-flow impact models, based on a small scale modelling approach. Surv Geophys 34(1):121–140

Tang JB, Hu KH, Zhou GD et al (2013) Mud–rock flow impact pressure signal processing by the wavelet analysis. J Sichuan Univ (Eng Sci Ed) 45(1):8–13 **(In Chinese, with English abstract)**

Valentino R, Barla G, Montrasio L (2008) Experimental analysis and micromechanical modelling of dry granular flow and impacts in laboratory flume tests. Rock Mech Rock Eng 41(1):153–177

Wei H (1996) Experimental study on impulsive forces of mud–rock flow heads. China Railw Sci 17(3):50–62 **(In Chinese, with English abstract)**

Wendeler C, Volkwein A, Roth A et al (2007) Field measurements used for numerical modelling of flexible debris flow barriers. In: The fourth international conference on Debeis-flow hazards mitigation: mechanics, prediction, and assessment (The fourth international conference on debris flows)

Wu JS, Kang ZC, Tian LQ, Zhang SC (1990) Observation and research of Jiangjia Ravine in Yunnan. Science Press, Beijing

Wu JS, Tian LQ, Kang ZC et al (1993) Debris flow and its comprehensive control. Science Press, Beijing

Yang HJ, Wei FQ, Hu KH et al (2011) Measuring the internal velocity of debris flows using impact pressure detecting in the flume experiment. J Mt Sci 8:109–116

Yu XB, Chen XQ, Chen JG (2018) Impulsive forces distribution along the sediment storage dam upstream face for different mud–rock flow unit weight. Environ Earth Sci 77(5):1–15

Zeng C (2014) Vulnerability assessment of building to mud–rock flow hazard. Graduate University of Chinese Academy of Sciences

Zeng C, Su ZM, Lei Y et al (2015) An experimental study of the characteristics of impact forces between debris flow slurry and large-sized particles. Rock Soil Mech 36(7):1923–1930+1938

Zhang SC, Yuan JM (1985) Mud-rock flow impact and its test, vol 4. Lanzhou Institute of Glaciology and Cryopedology, Chinese Academy of Sciences, Beijing, pp 269–274